# Kinetic Energy Budget for the Madden–Julian Oscillation in a Multiscale Framework

LEI ZHOU

*Lamont-Doherty Earth Observatory, Columbia University, New York, New York, and State Key Lab of Satellite Ocean Environment Dynamics, SIO, SOA, Hangzhou, China*

ADAM H. SOBEL

*Department of Applied Physics and Applied Mathematics, and Department of Earth and Environmental Sciences, and Lamont-Doherty Earth Observatory, Columbia University, New York, New York*

RAGHU MURTUGUDDE

*Earth System Science Interdisciplinary Center, University of Maryland, College Park, College, Park, Maryland*

(Manuscript received 17 June 2011, in final form 8 February 2012)

ABSTRACT

A kinetic energy budget for the Madden–Julian oscillation (MJO) is established in a three-scale framework. The three scales are the zonal mean, the MJO scale with wavenumbers 1–4, and the small scale with wavenumbers larger than 4. In the composite budget, the dominant balance at the MJO scale is between conversion from potential energy and work done by the pressure gradient force (PGF). This balance is consistent with the view that the MJO wind perturbations can be viewed as a quasi-linear response to a slowly varying heat source. A large residual in the upper troposphere suggests that much kinetic energy dissipates there by cumulus friction. Kinetic energy exchange between different scales is not a large component of the composite budget. There is a transfer of kinetic energy from the MJO scale to the small scale; that is, this multiscale interaction appears to damp rather than strengthen the MJO. There is some variation in the relative importance of different terms from one event to the next. In particular, conversion from mean kinetic energy can be important in some events. In a few other events, the influence from the extratropics is pronounced.

## 1. Introduction

The Madden–Julian oscillation (MJO) is the dominant mode of intraseasonal variability in the tropics (Madden and Julian 1971, 1972, 1994). There have been many theories and model studies of the MJO thus far, as summarized in Wang (2005) and Slingo et al. (2005). Different theories focus on different mechanisms, such as wave–conditional instability of the second kind (CISK) (e.g., Lindzen 1974; Lau and Peng 1987), upscale cascade from small-scale convection (Moncrieff 2004; Majda 2007a,b), recharge–discharge (e.g., Blade and Hartmann 1993; Hu and Randall 1995; Kemball-Cook and Weare 2001; Sobel and Gildor 2003), feedbacks with surface heat fluxes and radiation (e.g., Emanuel 1987; Neelin et al. 1987; Raymond 2001; Sobel et al. 2008, 2010), and interactions with synoptic scales (Biello and Majda 2005; Biello et al. 2007).

In this study, we examine the MJO from the point of view of the kinetic energy budget, constructed from reanalysis datasets. The results can be used to provide some constraints on theory, though they do not clearly validate or rule out any specific theory that has been proposed. Analysis of the budget for individual events can shed light on the differences between events as well as the features common to most of them.

The Lorenz energy cycle (Lorenz 1955; Holton 2004) is a well-known quantitative framework within which to study energy and its transformation in the atmosphere. However, it was established for the midlatitudes. Thus, some assumptions are not suitable for the tropics, for example, the neglect of vertical fluxes (advection terms by the vertical velocity in the momentum equations). In addition, the MJO has been hypothesized to involve processes at multiple scales. For example, Biello and

*Corresponding author address:* Lei Zhou, 301d Oceanography, Lamont-Doherty Earth Observatory, 61 Route 9W, Palisades, NY 10964.
E-mail: lzhou@ldeo.columbia.edu

DOI: 10.1175/JCLI-D-11-00339.1

Majda (2005) established a multiscale model in which both the upscale and downscale energy transfer associated with the MJO are important. We construct a set of energy equations from the primitive equations by adopting assumptions suitable for the tropics. We will focus our discussion on the energy conversion related to the MJO. It is impossible to construct a completely closed budget for kinetic energy from reanalysis datasets because of the lack of some key variables (such as friction, convective heating, and other unresolved subgrid processes). Our discussion focuses on the dominant terms in the energy budget that are resolved in the reanalyses; regions in which the residual is significant are discussed specifically.

Derivation of the energy equation is described in section 2. Definition of the composite MJO event in this study is described in section 3. Detailed results for every term in the composite energy equation are presented in section 4. Case studies on some special MJO events, in which the dominant balance is different from that in the composite, are presented in section 5. Finally, a summary is offered in section 6.

## 2. Kinetic energy equation in three scales

The primitive equations on the $\beta$ plane in isobaric coordinates are

$$\left(\frac{\partial}{\partial t} + u\frac{\partial}{\partial x} + v\frac{\partial}{\partial y} + \omega\frac{\partial}{\partial p}\right)u - \beta y v = -\frac{\partial \Phi}{\partial x} + X, \quad (1a)$$

$$\left(\frac{\partial}{\partial t} + u\frac{\partial}{\partial x} + v\frac{\partial}{\partial y} + \omega\frac{\partial}{\partial p}\right)v + \beta y u = -\frac{\partial \Phi}{\partial y} + Y, \quad (1b)$$

$$\frac{\partial u}{\partial x} + \frac{\partial v}{\partial y} + \frac{\partial \omega}{\partial p} = 0, \quad \text{and} \quad (1c)$$

$$\frac{\partial \Phi}{\partial p} = -\frac{RT}{p}, \quad (1d)$$

where $u$, $v$, and $\omega$ are zonal, meridional, and vertical velocities; $\beta$ is the meridional gradient of the Coriolis parameter; $\Phi$ is the geopotential; $T$ is the temperature; while $X$ and $Y$ are residuals denoting all unresolved processes. We develop a spectral multiscale framework consisting of three components: 1) the zonal mean component (wavenumber zero); 2) the MJO scale (zonal wavenumbers 1–4); and 3) "small-scale" processes that have zonal wavenumbers higher than 4. The latter may include, but are not restricted to, convectively coupled equatorial waves (CCEW; Kiladis et al. 2009). This decomposition into three scales is supported by the wavenumber spectra of key dynamic and thermodynamic variables, as shown in Fig. 1a. The wavenumber in Fig. 1a starts from $k = 1$. Taking zonal winds at 850 hPa (the green line in Fig. 1a), for example, wavenumber spectra are computed for the meridionally averaged (between 10°N and 10°S) zonal winds for every day and then averaged together. The result is normalized by the corresponding 95% significance level (the number of degrees of freedom is taken to be 68, estimated as $2 \times (N/n)$, where $N = 8644$ is the record length, and $n = 256$ is the FFT length; Taylor 1921; Leith 1973). Finally, the normalized wavenumber spectra for the days during MJO events, which are defined based on a multivariate MJO index (Wheeler and Hendon 2004; referred to as WH04 hereafter; see Section 3 for details), are averaged; the mean spectrum is presented in Fig. 1a. Where the normalized spectrum in Fig. 1a is larger than 1, the peak is significant at the 95% significance level and persists in time during the MJO. For all variables, there are significant peaks around wavenumber 3, but none between wavenumber 5 and wavenumber 10. There are also some significant peaks with wavenumbers higher than 10, but they are not consistent in all variables. The wavenumber range for the MJO is chosen to be 1–4 because this is a well-documented feature of the MJO (see, e.g., Zhang 2005). Our selection remains consistent with previous

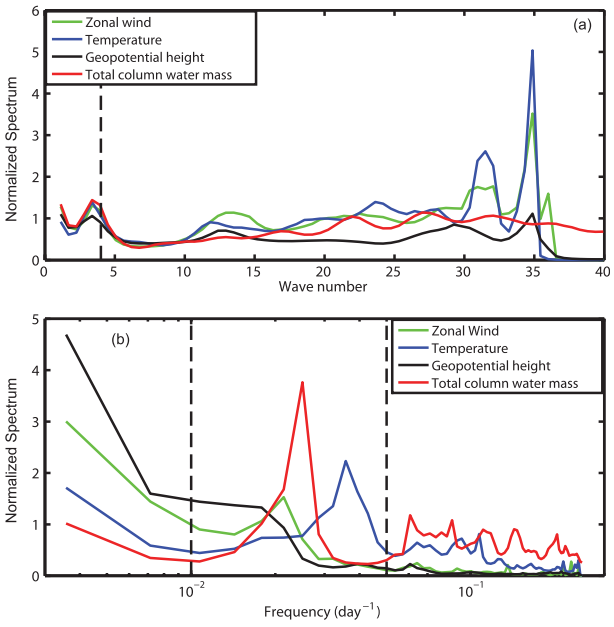


FIG. 1. (a) Wavenumber spectra of zonal winds at 850 hPa, air temperatures at 850 hPa, geopotential heights at 850 hPa, and total column water mass. All variables are averaged between 10°N and 10°S before the spectra are calculated. All spectra are normalized by the corresponding 95% confidence level. Wavenumber 4 is marked with a dash line. (b) Power spectra of the above variables, which are also normalized by the corresponding 95% confidence level. Frequencies at 1/100 day$^{-1}$ and 1/20 day$^{-1}$ are marked with dash lines.

studies. Nevertheless, there is a wide gap between the MJO scale and the small scale (between wavenumber 5 and wavenumber 10). Actually, we can set the cutoff wavenumber within this gap and the following results are not sensitive to this selection. The purpose of showing these spectra in Fig. 1a is not to quantitatively determine all spectral peaks, but to verify that the MJO scale (wavenumbers 1–4) is distinct from variability with higher wavenumbers. The rapid drop at large $k$ in the zonal wind spectrum (the green line in Fig. 1a) is due to the inability of the reanalysis products to resolve zonal winds with wavelengths smaller than 800–1000 km (Milliff et al. 2004).

Given that the spatial scales are distinct, all variables are decomposed into three components. Taking the zonal velocity $u$ for example, the zonal mean is denoted with $\overline{u}$. After removing the zonal mean, the zonal wind at the MJO scale (denoted $u'$) and the zonal wind at the small scale (denoted $u''$) are reconstructed from the corresponding Fourier components. Thus, the zonal velocity can be written as $u = \overline{u} + u' + u''$. In Eq. (1), all terms are linear except for the advection terms, which enable interactions between different scales. By analogy to the standard decomposition into two scales (mean and perturbation), the advection terms are categorized into three scales in the following way (see appendix A for technical details), taking the term $v\partial u/\partial y$, for example,

1) the equation for the zonal mean velocity includes $\overline{v}\partial\overline{u}/\partial y$, $\overline{v'\partial u'/\partial y}$, and $\overline{v''\partial u''/\partial y}$,
2) advection at the MJO scale consists of $[\overline{v}\partial u'/\partial y]$, $[v'\partial\overline{u}/\partial y]$, $[v''\partial u''/\partial y]$, and $[v'\partial u'/\partial y] - \overline{v'\partial u'/\partial y}$,
3) advection at small scales is comprised of $\overline{v}\partial u''/\partial y$, $v''\partial\overline{u}/\partial y$, $v'\partial u''/\partial y$, $v''\partial u''/\partial y$, and $v''\partial u''/\partial y - [v''\partial u''/\partial y]$;

where the overbar denotes the zonal mean, and [ ] denotes the average on the MJO scale. Here, $\overline{v'\partial u'/\partial y}$ and $[v''\partial u''/\partial y]$ are grouped into scales larger than the scale of the velocities themselves because these two terms represent the energy transfer from smaller scale to larger scale or upscale energy cascade. Considering these approximations and some additional manipulations as shown in appendix B, the kinetic energy equations at the MJO scale can be written as

$$\frac{\partial \mathrm{KE}'}{\partial t} = -\overline{\mathbf{u}}\cdot\nabla\mathrm{KE}' + [\mathrm{KE}'\times\mathrm{KE}''] + [\mathrm{KE}'\times\overline{\mathrm{KE}}] - \nabla\cdot(\mathbf{U}'\Phi') + [\mathrm{KE}'\times\mathrm{PE}'] + \mathrm{EV} + R, \quad (2)$$

where $\mathrm{KE}' = (u'^2 + v'^2)/2$ represents the kinetic energy on the MJO scale; $\nabla = (\partial/\partial x)\mathbf{i} + (\partial/\partial y)\mathbf{j} + (\partial/\partial p)\mathbf{k}$; and $\mathbf{U}' = u'\mathbf{i} + v'\mathbf{j} + \omega'\mathbf{k}$. In the following, all terms in Eq. (2) will be first calculated with reanalysis products at each grid point and at every time step. Thus, the terms do not have a bar over them in Eq. (2). For example, we use $(u'^2 + v'^2)/2$ instead of $\overline{(u'^2 + v'^2)}/2$. Then, the composite terms in the kinetic energy budget for the composite MJO event are calculated and the results are shown below. All terms are appropriately composited with respect to the MJO phases (defined in WH04) after having been computed from unfiltered data. The kinetic energy equations for the other two scales (the zonal mean and the small scale) can be obtained in the same way but are not the focus of this study and are not presented here. Physical interpretations of the terms in Eq. (2), which are analogous to the physical meanings of the corresponding terms in the Lorenz energy cycle (Holton 2004), are listed as follows.

1) $\partial\mathrm{KE}'/\partial t$ is the local tendency of KE′.
2) $-\overline{\mathbf{u}}\cdot\nabla\mathrm{KE}'$ is the advection of KE′ by zonal mean winds.
3) $[\mathrm{KE}'\times\mathrm{KE}'']$ denotes the kinetic energy conversion between the MJO scale (KE′) and the small scale (KE″). The explicit form is $-u'\nabla\cdot(u''\mathbf{U}'') - v'\nabla\cdot(v''\mathbf{U}'')$, $\mathbf{U}'' = u''\mathbf{i} + v''\mathbf{j} + w''\mathbf{k}$.
4) $[\mathrm{KE}'\times\overline{\mathrm{KE}}]$ denotes the kinetic energy conversion between the MJO scale (KE′) and the zonal mean scale ($\overline{\mathrm{KE}}$). The explicit form is $-u'(\mathbf{U}'\cdot\nabla\overline{u}) - v'(\mathbf{U}'\cdot\nabla\overline{v})$.
5) $\nabla\cdot(\mathbf{U}'\Phi')$ denotes the work done by the pressure gradient force (PGF).
6) $[\mathrm{KE}'\times\mathrm{PE}']$ denotes the energy conversion between the kinetic energy (KE′) and the potential energy (PE′) at the MJO scale. The explicit form is $-R\omega'T'/p$.
7) EV denotes the dot product of the MJO-scale velocity with the zonal eddy component of the MJO-scale momentum flux. The explicit form is

$$-u'\left[\left(u'\frac{\partial u'}{\partial x} - \overline{u'\frac{\partial u'}{\partial x}}\right) + \left(v'\frac{\partial u'}{\partial y} - \overline{v'\frac{\partial u'}{\partial y}}\right) + \left(\omega'\frac{\partial u'}{\partial p} - \overline{\omega'\frac{\partial u'}{\partial p}}\right)\right] - v'\left[\left(u'\frac{\partial v'}{\partial x} - \overline{u'\frac{\partial v'}{\partial x}}\right) + \left(v'\frac{\partial v'}{\partial y} - \overline{v'\frac{\partial v'}{\partial y}}\right) + \left(\omega'\frac{\partial v'}{\partial p} - \overline{\omega'\frac{\partial v'}{\partial p}}\right)\right].$$

8) The $R$ is the residual term with the explicit form of $u'X' + v'Y'$, which cannot be directly calculated with the resolved variables from the reanalysis products.

The total resolved energy source (denoted with TS hereafter) for the local kinetic energy tendency is defined as the sum from term 2 through term 7, that is,

$$\mathrm{TS} = -\overline{\mathbf{u}}\cdot\nabla\mathrm{KE}' + [\mathrm{KE}'\times\mathrm{KE}''] + [\mathrm{KE}'\times\overline{\mathrm{KE}}] - \nabla\cdot(\mathbf{U}'\Phi') + [\mathrm{KE}'\times\mathrm{PE}'] + \mathrm{EV}. \quad (3)$$

The residual terms $X$ and $Y$ are obtained from the momentum equation,

$$X = \left(\frac{\partial}{\partial t} + u\frac{\partial}{\partial x} + v\frac{\partial}{\partial y} + \omega\frac{\partial}{\partial p}\right)u - \beta y v + \frac{\partial \Phi}{\partial x}, \quad \text{and} \tag{4a}$$

$$Y = \left(\frac{\partial}{\partial t} + u\frac{\partial}{\partial x} + v\frac{\partial}{\partial y} + \omega\frac{\partial}{\partial p}\right)v + \beta y u + \frac{\partial \Phi}{\partial y}. \tag{4b}$$

Then, $X'$ and $Y'$ are the residual terms at the MJO scale, which have wavenumbers 1–4. All terms in the energy budget are calculated with the 40-yr European Centre for Medium-Range Weather Forecasts (ECMWF) Re-Analysis (ERA-40; Uppala et al. 2005) and National Centers for Environmental Prediction (NCEP)–National Center for Atmospheric Research (NCAR; Kalnay et al. 1996) reanalysis products. The two reanalysis yield qualitatively similar results. Most results presented in the following (sections 4 and 5) are obtained from ERA-40, unless otherwise specified.

Similarly, one can also construct the budget for MJO-scale potential energy (see appendix B) and a total energy budget for the MJO (including both kinetic and potential energy). The major source for PE′ is $R(J'T'/S_p p)$, where $J'$ is the diabatic heating, and $S_p$ is the static stability parameter. However, the diabatic heating, which is mainly due to convection, is not a standard output in reanalysis products. (In the operational analysis produced in the project, Year of Tropical Convection (YOTC), the diabatic heating is stored, but this product only starts from May 2008 and is too short to include enough MJO events for an analysis along the lines we present here.) Therefore, the potential energy budget is not discussed in detail here.

## 3. Composite Madden–Julian oscillation

We employ the MJO index defined by WH04 (http://www.bom.gov.au/climate/mjo/). The amplitudes of MJO events are determined from the sum of the squares of the first two leading principal components of the combined OLR and wind fields (i.e., MJO index = $\mathrm{RMM1}^2$ + $\mathrm{RMM2}^2$). A daily MJO index is used for this study. Significant MJO events are identified according to the criterion that the MJO index must be larger than two for a period longer than 30 days; the MJO index is permitted to be less than two for up to three days during the period without either disqualifying the event or causing it to be split into two. With this criterion, there are 35 MJO events in the period 1979–2009. The events are listed in Table 1. Our criterion allows only strong MJO events, which thus are fewer in number than would be obtained with lower thresholds. The lifetimes of the events in Table 1 range from 30 days (only 2 events) to 85 days, with a mean of 47 days. In a few MJO events with long durations (e.g., MJO event 18 has the longest lifetime, 85 days), intraseasonal signals can successfully go around the globe as a single event (Matthews 2008). Because we wish to select all MJO events with objective and uniform criteria, we do not manually separate these relatively long MJO events into two short ones.

TABLE 1. MJO events defined based on the MJO index of Wheeler and Hendon (2004) and the selection criteria in the main text.

| No. | Beginning date | End date | No. | Beginning date | End date |
|---|---|---|---|---|---|
| 1 | 2 Apr 1979 | 6 May 1979 | 19 | 15 Aug 1991 | 18 Sep 1991 |
| 2 | 14 May 1979 | 24 Jun 1979 | 20 | 30 Dec 1992 | 10 Feb 1993 |
| 3 | 1 Aug 1979 | 8 Sep 1979 | 21 | 2 Mar 1996 | 6 Apr 1996 |
| 4 | 21 Sep 1979 | 4 Nov 1979 | 22 | 5 Dec 1996 | 13 Jan 1997 |
| 5 | 18 Mar 1980 | 24 Apr 1980 | 23 | 4 Feb 1997 | 4 Apr 1997 |
| 6 | 12 Feb 1981 | 12 Apr 1981 | 24 | 14 May 1997 | 17 Jun 1997 |
| 7 | 27 Aug 1981 | 1 Oct 1981 | 25 | 10 Nov 2000 | 14 Dec 2000 |
| 8 | 22 Oct 1984 | 10 Dec 1984 | 26 | 8 Jan 2001 | 3 Mar 2001 |
| 9 | 10 Jan 1985 | 16 Mar 1985 | 27 | 28 Apr 2002 | 20 Jul 2002 |
| 10 | 21 Oct 1985 | 22 Nov 1985 | 28 | 27 Oct 2002 | 7 Dec 2002 |
| 11 | 28 Dec 1985 | 31 Jan 1986 | 29 | 9 May 2003 | 23 Jun 2003 |
| 12 | 25 Feb 1986 | 5 Apr 1986 | 30 | 5 Dec 2003 | 10 Feb 2004 |
| 13 | 25 Oct 1986 | 29 Nov 1986 | 31 | 18 Jun 2004 | 17 Jul 2004 |
| 14 | 14 May 1987 | 12 Jun 1987 | 32 | 16 Mar 2005 | 22 May 2005 |
| 15 | 27 Jul 1987 | 31 Aug 1987 | 33 | 21 Sep 2006 | 21 Oct 2006 |
| 16 | 12 Feb 1988 | 17 Apr 1988 | 34 | 15 Nov 2007 | 26 Jan 2008 |
| 17 | 24 Dec 1989 | 18 Feb 1990 | 35 | 26 Mar 2009 | 5 May 2009 |
| 18 | 25 Feb 1990 | 20 May 1990 | | | |

Atmospheric intraseasonal oscillations of all types were carefully categorized by Wang and Rui (1990, hereafter referred to as WR90). Mathematically, the above criteria along with the WH04 MJO index do not necessarily discriminate between the eastward- and westward-propagating signals; but in practice, eastward-propagating events are primarily selected because it is these that project most commonly on the combined EOF structures that are used to derive the index. For example, event 9 (Table 1) is the same as the one shown in WR90 (their Fig. 1). However, the independent northward-propagating events (e.g., Sep 18, 1984 – Oct 17, 1984; Fig. 6 in WR90) and the westward-propagating events (e.g., 19 August 1982–12 September 1982; Fig. 9 in WR90) are excluded. Since the westward-propagating signals are not preferred in the WH04 MJO index, the interactions between eastward-propagating signals (with positive wavenumbers) and westward-propagating signals (with negative wavenumbers), which have the same wavenumbers but opposite signs, are not pronounced. As a result, the projection from the MJO scale onto the zonal mean scale due to such interactions is negligible.

Our composite MJO events are displayed using the Hovmöller diagram of the composite of each meridionally and vertically averaged term (between 10°N and 10°S; through the troposphere from 1000 to 100 hPa) in the kinetic energy budget. Usually, there are two convection centers, identified by negative OLR anomalies, during an MJO event in the Indo-Pacific region: one in the central Indian Ocean and the other in the western Pacific Ocean. Two central points are chosen along the equator, one at 80°E and the other at 130°E. For each convection center, the day when the OLR anomaly reaches its minimum is chosen as day 0. Then, 30 days before and after day 0 are taken from all MJO events (Table 1) to make the composite Hovmöller diagrams. The results for the two convection centers are qualitatively the same, thus only those constructed for 80°E are shown below.

## 4. Results for composite MJO event

### *Kinetic energy at the MJO scale*

The Hovmöller diagram of the composite KE′ is shown in Fig. 2. The significance of the composite signal is tested against the background variation. For each grid point, we define $R = (\mathrm{KE}'_{\mathrm{composite}} - \mathrm{KE}'_{\mathrm{mean}})/\mathrm{KE}'_{\mathrm{std}}$, where $\mathrm{KE}'_{\mathrm{composite}}$ is the mean kinetic energy over all MJO days, $\mathrm{KE}'_{\mathrm{mean}}$ is the climatological mean of KE′ over all days from 1979 to 2002, and $\mathrm{KE}'_{\mathrm{std}}$ is the standard deviation (STD) of KE′ over all days from 1979 to 2002. If $R$ is larger than 1 (smaller than $-1$), the composite at this grid point is significantly larger (smaller) than the background variation. For other terms in the kinetic energy budget (shown in the following figures), the significance of the composite will also be tested with the ratio $R$, which is defined analogously. In Fig. 2, the white contours mark the regions where $R$ is larger than 1, since KE′ is always positive.

Figure 2 shows that a broad maximum in kinetic energy propagates from the Indian Ocean to the western Pacific Ocean during the composite MJO event, coherent with the OLR minimum. The KE′ maximum lags the OLR minimum in longitude and time, and is stronger over the Pacific than the Indian Ocean in both composites. Positive TS [the total resolved energy source defined in Eq. (3)] occurs a few days before the enhanced KE′ (Fig. 3). The advection of KE′ by the zonal mean winds is small (not shown). The dominant energy source for $\partial \mathrm{KE}'/\partial t$ in the kinetic energy budget is the energy gain from PE′ via the term [KE′ × PE′], which is shown in Fig. 4. Positive [KE′ × PE′] occurs to the east rather than to the west of the convection center. Since the location of the greatest energy source and that of maximum kinetic energy do not match, some process must be transporting the gained kinetic energy from one location to the other.

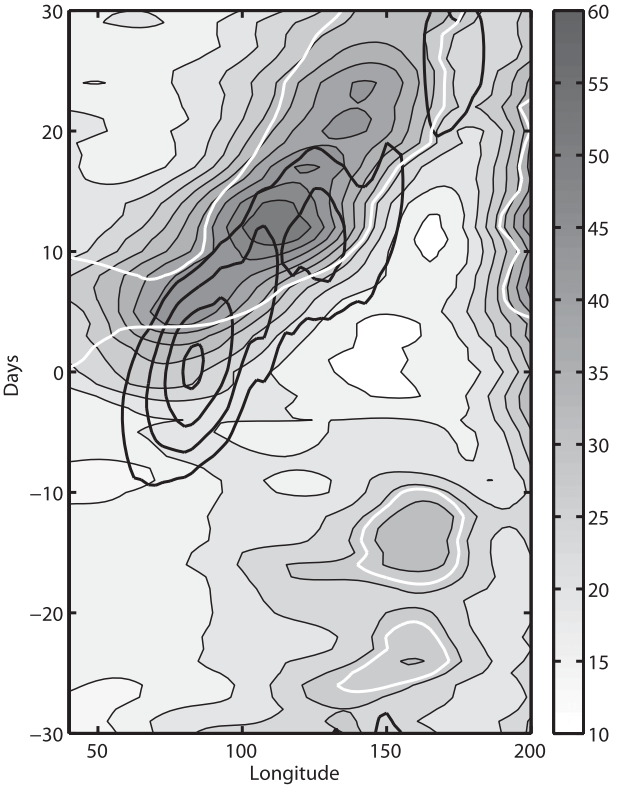


FIG. 2. Hovmöller diagram of KE′ (averaged between 10°N and 10°S, from 1000 to 100 hPa) during the composite MJO event. Day 0 is that of minimum OLR anomaly at 80°E. The thin contours are from 10 to 60 J kg$^{-1}$ with an interval of 5 J kg$^{-1}$. The thick black contours show negative intraseasonal OLR anomalies, starting from $-10$ W m$^{-2}$ with an interval of 10 W m$^{-2}$. White contours mark the region where the energy conversion is significant ($R > 1$; see the text for the definition of $R$).

This is the PGF; the term $-\nabla \cdot (\mathbf{U}'\Phi')$, as shown in Fig. 5 (Yanai et al. 2000). The dipole structure, with negative work done by PGF to the east of the convection center and positive work farther west, represents westward transport of the kinetic energy. As a result, KE′ is greatest to the west of the convection center (Fig. 3).

Although the two largest terms in the kinetic energy budget at the MJO scale, [KE′ × PE′] and $-\nabla \cdot (\mathbf{U}'\Phi')$, tend to compensate each other, their sum is still a dominant term in the budget. Since both [KE′ × PE′] and $-\nabla \cdot (\mathbf{U}'\Phi')$ are part of the linear terms in the momentum equations [Eq. (1)], the balance between these two terms indicates that the kinetic energy associated with MJO events is mainly controlled by linear processes, at least in the coarse view offered by the vertically and meridionally integrated kinetic energy budget. The horizontal structures of the most important terms (averaged between 1000 and 100 hPa in the vertical and over all MJO days) in the kinetic energy budget are shown in Figs. 6a and 6b. Positive [KE′ × PE′] and

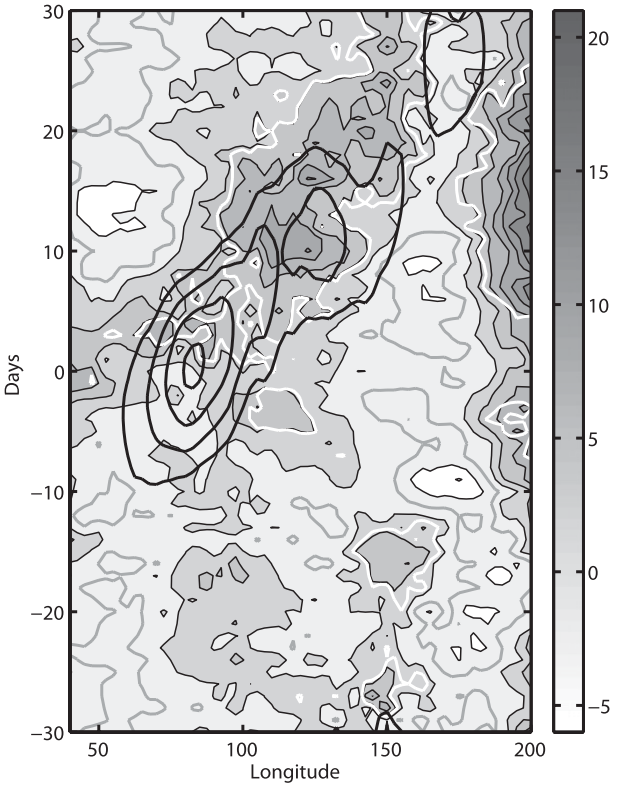


FIG. 3. As in Fig. 2, but for the total energy source [TS in Eq. (3)]. The interval for the thin contours is 3 J day$^{-1}$ kg$^{-1}$. The gray contours represent zero. The thick black contours show negative intraseasonal OLR anomalies, starting from −10 W m$^{-2}$ with an interval of 10 W m$^{-2}$. White contours mark the region where the energy conversion is significant ($R > 1$).

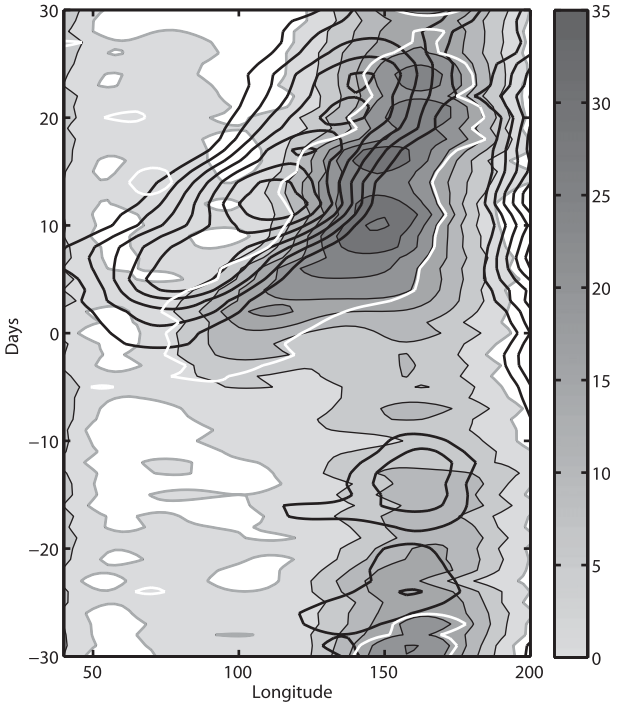


FIG. 4. As in Fig. 2, but for the energy conversion between KE′ and PE′ via [KE′ × $PE'$]. The interval for the thin contours is 5 J day$^{-1}$ kg$^{-1}$. The gray contours correspond to zero. The thick black contours show the kinetic energy (KE′) from 10 to 60 J kg$^{-1}$ with an interval of 5 J kg$^{-1}$. White contours mark the region where the energy conversion is significant ($R > 1$).

negative $-\nabla \cdot (\mathbf{U}'\Phi')$ are collocated in the tropics from the central Indian Ocean to the western Pacific Ocean (Fig. 6b). Their sum is shifted to the west, with the largest values found in the central Indian Ocean where the kinetic energy of the MJO also reaches its maximum (Fig. 6a).

The compensation between [KE′ × PE′] and the work done by PGF also holds in the classical Gill model (Gill 1980). From numerical solutions using the code of Bretherton and Sobel (2003; parameter values are listed in Table 2), the energy budget is shown in Figs. 6c and 6d. The perturbed kinetic energy is shown in Fig. 6c with black contours. In this idealized model, since the only energy source is the heating (denoted $M$, see Bretherton and Sobel (2003) for more details) centered on the origin of the domain, the energy source is proportional to $M \times \phi$. This quantity maximizes around the center of the domain (black contours in Fig. 6d). The energy source is compensated by the work done by PGF (white contours and shades in Fig. 6b) and the energy is shifted mainly to the west of the energy source (a small amount of energy is also shifted to the east). The sum of $M \times \phi$ and $-[\partial(u\phi)/\partial x] - [\partial(v\phi)/\partial y]$ (white contours and shades in Fig. 6c) is consistent with the enhanced energy (black contours in Fig. 6c). This similarity between the linear Gill-type model and major energy balance for the composite MJO event suggests that the linear dynamics of a forced, steady response to heating is relevant to the MJO, at least qualitatively.

Some previous studies (e.g., Nitta 1972; Lau and Lau 1992; Maloney and Dickinson 2003) have found that synoptic-scale tropical waves, though not stationary, share with the Gill model the feature that wave-scale kinetic energy is produced from wave-scale potential energy, which in turn is generated by diabatic heating. These wave-scale disturbances are classified as ''small scale'' in our framework, separated from the MJO scale both in space and time as shown in Fig. 1. Our analysis confirms that the same energetics, found also in the Gill model, is relevant to the MJO too. Similar conclusions have been reached by previous investigators (e.g., Hendon and Salby 1994; Sugiyama 2009). The assumption that the MJO wind anomalies are a quasi-steady response to heating is built into the idealized model of Sobel and Maloney (2012) explicitly, allowing the wind to be

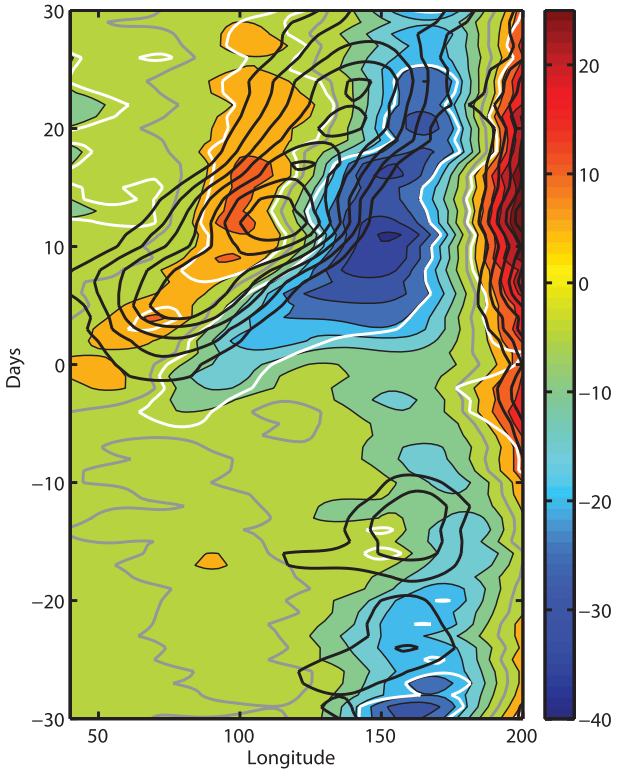


FIG. 5. As in Fig. 2, but for the term $\nabla \cdot (\mathbf{U}'\Phi')$. The interval for thin contours is 5 J day$^{-1}$ kg$^{-1}$. The gray lines are zero contours. The thick black contours show the kinetic energy (KE′) from 10 to 60 J kg$^{-1}$ with an interval of 5 J kg$^{-1}$. White contours mark the region where the energy conversion is significant ($R > 1$ and $R < -1$).

computed from the heating without using explicit solution of a momentum equation.

Both [KE′ × PE′] and the work done by PGF are energy conversions at the same scale, that is, the MJO scale. Term EV in Eq. (2) is also due to perturbations on the MJO scale. It projects on all scales, but is small on the MJO scale, and is not shown separately though it is included in the total source (TS) (shown in Figs. 3 and 12). The finding that this term is small is consistent with previous studies such as Lau and Lau (1992), Maloney and Dickinson (2003), and Seiki and Takayabu (2007).

In addition to energy conversions on the MJO scale, energy can also be exchanged between different scales. The energy conversion between KE′ and $\overline{\text{KE}}$ is shown in Fig. 7. Positive energy conversion indicates a gain by KE′ from the zonal mean field. However, this energy exchange is one order of magnitude smaller than the two dominant terms discussed above. It is also smaller than the sum of the two dominant terms. Thus, this term is not important in the composite MJO event. It may be important in a few specific MJO events, as discussed in section 5b.

The conversion between KE′ and KE″ is shown in Fig. 8. The pattern is noisy, since the scale of KE″ is small, but the fact that almost all values are negative indicates that the kinetic energy transfer is predominantly from the MJO scale to the small scale rather than the converse. The white contours in Fig. 8 mark the regions where $R$ (defined analogously as described above for KE′, just replacing KE′ with [KE′ × KE″]) is smaller than −1, since most [KE′ × KE″] is negative. It is clear that most regions of negative energy conversion between KE′ and KE″ during the composite MJO event are statistically significant. According to these calculations, the small-scale KE″ does not contribute significantly to the generation of MJO-scale kinetic energy (KE′) during the composite MJO event. Instead, it is a sink for the kinetic energy associated with the MJO.

In some theoretical studies such as Biello and Majda (2005) and Biello et al. (2007), upscale momentum transfer from synoptic-scale disturbances to the MJO scale plays an important role. These studies did not address the energetics explicitly, and the planetary-scale wind fields in their models are driven both by upscale energy transfers from synoptic-scale disturbances and direct heating at the planetary scale. It is beyond the scope of this study to perform a detailed evaluation of these or any other specific theories in light of our results. Our results do indicate, however, that upscale transfers of kinetic energy directly from synoptic to planetary scales are not responsible for the overall generation of vertically and meridionally integrated kinetic energy on the MJO scale in most events, to the extent that the reanalysis can address the question. As such upscale kinetic energy transports must be associated with upscale momentum transports, statements such as that of Biello and Majda (2005) that the "westerly midlevel inflow in the strong westerly region and the quadrupole vortex are largely produced in the model by the upscale transport of momentum to the planetary scales, while the midlevel easterly jet in the westerly onset region is substantially strengthened by this process" are, at least, not obviously supported by our results, inasmuch as we expect the westerly inflow and quadrupole vortex to be the dominant contributors to the planetary-scale kinetic energy of the MJO.

Another multiscale process of potential importance is convective momentum transport (CMT; Lin et al. 2005; Tung and Yanai 2002; Zhou et al. 2012; Miyakawa et al. 2012). The convective and mesoscale motions presumably responsible for CMT are not resolved in either ERA-40 or NCEP because of their coarse spatial resolution. Thus, the interaction between KE′ and KE″ discussed above is not CMT. CMT is represented in this study only as part of a residual, shown below.

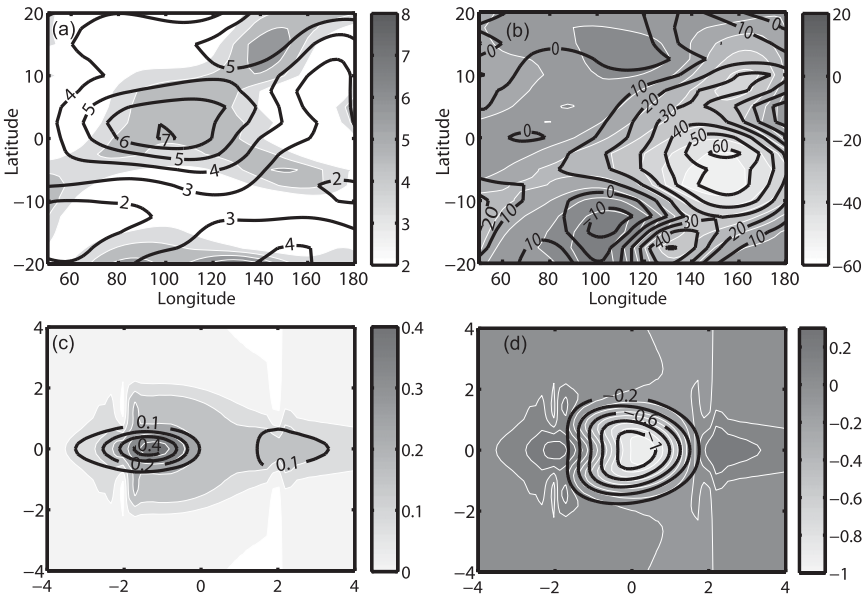


FIG. 6. (a) Gray shades and white contours: $[KE' \times PE'] - \nabla \cdot (\mathbf{U}'\Phi')$ (units: J day$^{-1}$ kg$^{-1}$). Black contours: KE′ (units: ×10 J kg$^{-1}$). (b) Gray shades and white contours: $-\nabla \cdot (\mathbf{U}'\Phi')$. Black contours: [KE′ × PE′] (units: J day$^{-1}$ kg$^{-1}$). The quantities shown in (a),(b) are vertically averaged from 1000 to 100 hPa and through all days during the MJO events listed in Table 1. (c) Kinetic energy (the black contours) and $M \times \phi - \partial(u\phi)/\partial x - \partial(v\phi)/\partial y$ (white contours and gray shades), where $M$ is the heating and $\phi$ is the geopotential. (d) $M \times \phi$ (the black contours), which is the energy source for the potential energy and $-\partial(u\phi)/\partial x - \partial(v\phi)/\partial y$ (white contours and gray shades), which redistributes the energy obtained from potential energy. Energy budget in the Gill-type model of Bretherton and Sobel (2003) is shown in (c),(d).

The vertical profile of KE′ at 80°E averaged between 10°N and 10°S during the composite MJO event is shown in Fig. 9. Day 0 is the day when the OLR anomalies reach their minima at 80°E. Kinetic energy has maxima at two levels. One is around 800 hPa on day 5 (after the convection) because of the MJO westerly phase or westerly wind burst. The other is around the tropopause, associated with the easterly winds there. As discussed above, the primary energy source for KE′ is conversion from PE′, which occurs a few days before the convection on day 0 (white contours in Fig. 10). This conversion is greatest between 500 and 200 hPa, the levels with largest convective heating (e.g., Houze 1982; Schumacher et al. 2004). However, these levels are not the same as those with the greatest KE′ in Fig. 9. The energy obtained from PE′ is transferred by the PGF as shown with the color shades in Fig. 10. Around 400 hPa and a few days before the convection, one can see negative work done by the PGF, which compensates the energy gained from PE′. PGF transfers the energy both upward to 200 hPa and downward to ~700 hPa, which are the levels of greatest KE′. Since the other terms in the energy budget for the composite MJO event are much smaller than the two terms shown in Fig. 10, they are not shown here.

In the lower troposphere, there is a three-way balance between the terms $-\nabla \cdot (\mathbf{U}'\Phi')$, [KE′ × PE′], and [KE′ × KE″] as shown in Fig. 11. Downward energy transfer by PGF is the primary energy source for KE′ (Fig. 11a). The main sink of KE′ is the energy conversion to KE″ (Fig. 11c). There is negative conversion back to PE′ around 600 hPa (Fig. 11b). There is also a weak source of KE′ below 800 hPa via [KE′ × PE′], perhaps due to shallow convection (Fig. 11b), but this does not vary with the composite MJO phase. The net result of this three-way balance provides kinetic energy to the westerly wind burst in the lower troposphere (Fig. 9). Conversion from potential energy is greatest in the upper

TABLE 2. Parameters for the numerical solutions to the Gill-type model in a rectangular domain, using the code of Bretherton and Sobel (2003). The Rayleigh damping rate and the Newtonian cooling rate are normalized by $\sqrt{\beta c}$, where $c = 50$ m s$^{-1}$. The heating has the form $M = \cos\{[(x - x_0)/2L_x]\pi\} \exp[-(y - y_0)^2/2L_y^2]$, where $x_0 = 0$, and $y_0 = 0$. When $x - x_0 > L_x$ or $x - x_0 < -L_x$, $M = 0$. The length scale for $X$ domain, $Y$ domain, $L_x$, and $L_y$ is $\sqrt{c/\beta}$.

| Rayleigh damping rate | Newtonian cooling rate | $X$ domain | $Y$ domain | $L_x$ | $L_y$ |
|---|---|---|---|---|---|
| 0.0001 | 0.0001 | −10 to 10 | −10 to 10 | 2 | 1 |

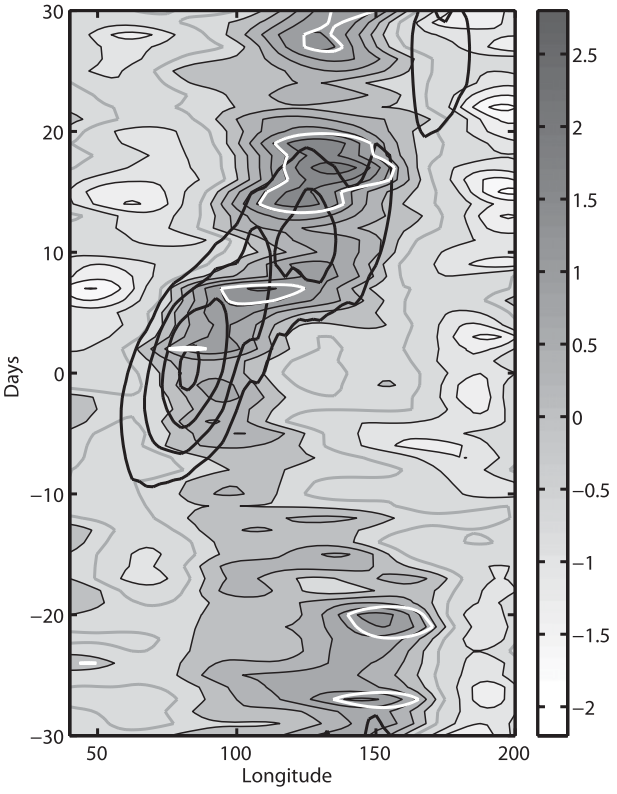


FIG. 7. As in Fig. 2, but for $KE' \times \overline{KE}$. The interval for the thin contours is 0.4 J day$^{-1}$ kg$^{-1}$. Zero is shown with gray contours. The thick black contours show negative intraseasonal OLR anomalies, starting from $-10$ W m$^{-2}$ with an interval of 10 W m$^{-2}$. White contours mark the region where the energy conversion is significant ($R > 1$).

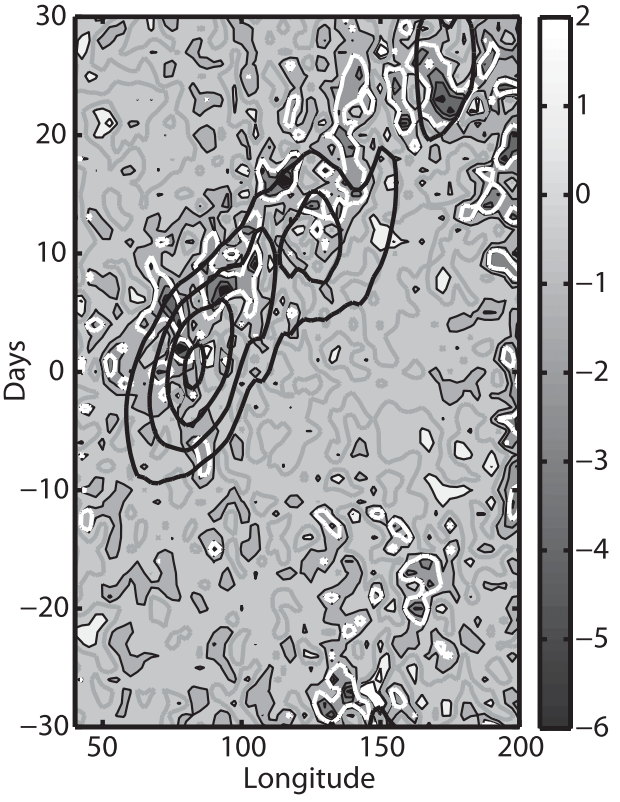


FIG. 8. As in Fig. 2, but for [$KE' \times KE''$]. Negative values means energy is transferred from KE′ to KE″. Thick gray contours correspond to zero. The interval of thin black contours is 1 J day$^{-1}$ kg$^{-1}$. White contours mark the region where the energy conversion is significant ($R < -1$). The thick black contours show negative OLR anomalies, starting from $-10$ W m$^{-2}$ with an interval of 10 W m$^{-2}$.

troposphere, but the PGF transports it downward into the westerly wind burst, where it is lost from the MJO scale in part by conversion to smaller-scale motions.

The total energy source [TS defined in Eq. (3)] is shown in Fig. 12a. In most of the domain, the residuals are very small, indicating the approximate closure of resolved terms in the reanalysis products. However, there are large residuals in the upper troposphere (around 200 hPa), which are greatest for a few days following the peak convection. These positive residuals are assumed to be compensated by the residual term $u'X' + v'Y'$ (Fig. 12b), a large fraction of which is presumably associated with cumulus momentum transport (CMT; Tung and Yanai 2002; Lin et al. 2005). The sum of the total resolved energy source (TS in Fig. 12a) and the residual terms (Fig. 12b) is given in Fig. 12c. In the upper troposphere (~200 hPa), a positive tendency, which leads to an increase of KE′, lasts from about day −5 to about day 7. A negative tendency occurs after this time and KE′ decreases. In the lower troposphere (between 800 and 600 hPa), there is a positive tendency around day 4. The pattern of the total tendency of KE′ in Fig. 12c explains the variation of KE′ shown in Fig. 9. Large cumulus friction in the upper troposphere is consistent with the zonal momentum budget presented by Lin et al. (2005). The influence of this significant cumulus friction on MJO dynamics has not been studied carefully to our knowledge and is worthy of further investigation.

Equation (2) for the kinetic energy budget at the MJO scale is obtained with the variables decomposed in the zonal direction (see appendix B for details). The variables can also be decomposed with respect to time. We follow a three-scale framework analogous to that used for the spatial decomposition above. The first and the most slowly varying component is defined by the use of a low-pass filter (Butterworth digital filter) with a cutoff period of 100 days; the second is the intraseasonal component, with periods between 20 and 100 days; and the third one is the high-frequency component with periods shorter than 20 days. The validity of the scale separation is tested with normalized power spectra of major dynamic

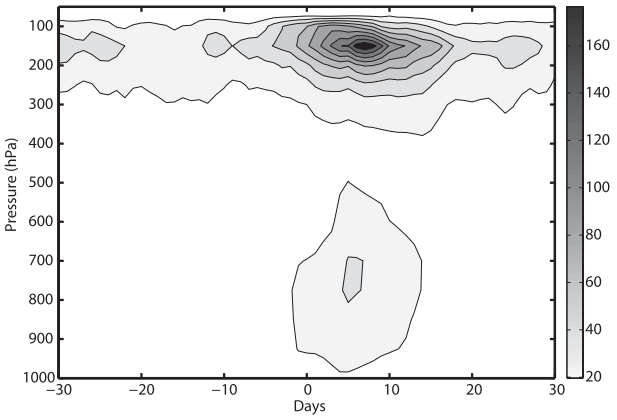


FIG. 9. Vertical profile of composite KE′ at 80°E averaged between 10°N and 10°S. Day 0 is the day when the OLR anomalies reach the minimum at 80°E (units: J kg$^{-1}$).

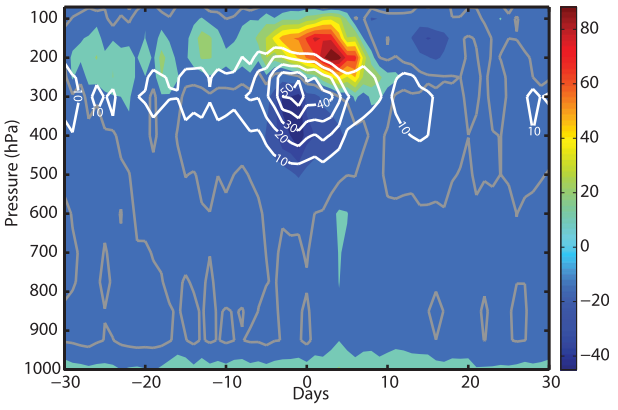


FIG. 10. As in Fig. 9, but for [KE′ × PE″] with white contours and for $-\nabla\cdot(\mathbf{U}'\Phi')$ with color shading (units: J day$^{-1}$ kg$^{-1}$).

and thermodynamic variables (Fig. 1b). The zonal wind at 850 hPa (the green line in Fig. 1b), for example, is averaged between 10°N and 10°S. The power spectrum thus calculated at each longitude is averaged between 50°E and 180° (over the whole Indian Ocean and the western Pacific Ocean) and the averaged spectrum is normalized by the corresponding 95% significance level (the number of degrees of freedom is taken to be 80, determined in the same way as for Fig. 1a). Intraseasonal peaks for various variables are clearly seen in Fig. 1b. The frequency of the intraseasonal peak for temperature (the blue line in Fig. 1b) is higher than we might normally consider for the MJO, but still within the intraseasonal band. The spectra with respect to time are calculated using the reanalysis products for all days and no a priori bandpass filtering is applied; in particular, they are not averaged only for the days during MJO events, as was done for the spatially filtered analysis above (i.e., Fig. 1a).

Taking $u$ for example, the variable can be written as $u = \overline{u} + u' + u''$, using the same notation for the three scales as in the spatial decomposition, though the overbar refers to low frequencies, the single prime to intraseasonal frequencies, and the double prime to high frequencies. Following a similar mathematical procedure to that in appendix B, the kinetic energy budget equation at the intraseasonal scale has exactly the same form as Eq. (2). The physical interpretations of the terms

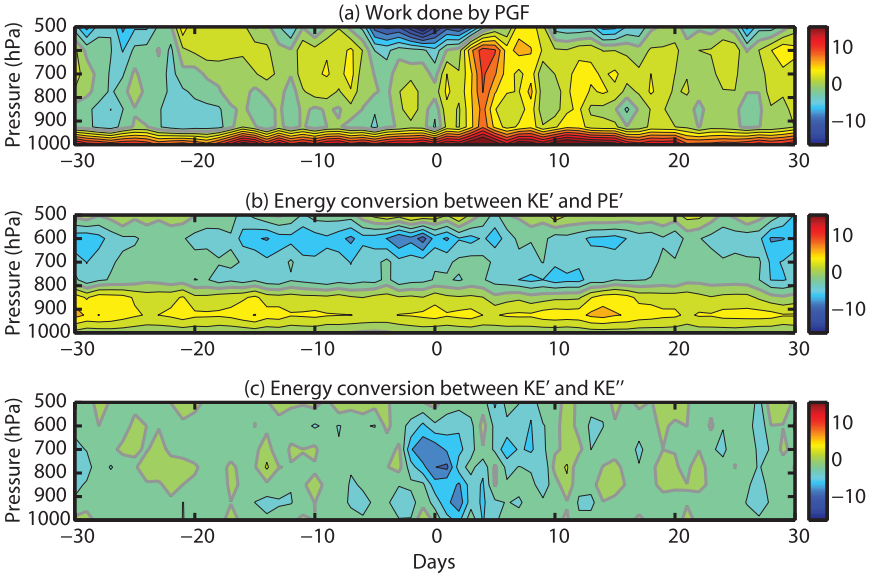


FIG. 11. As in Fig. 9, but for (a) $-\nabla\cdot(\mathbf{U}'\Phi')$ (b) [KE′ × PE″], and (c) [KE′ × KE″] in the lower troposphere below 500 hPa (units: J day$^{-1}$ kg$^{-1}$).

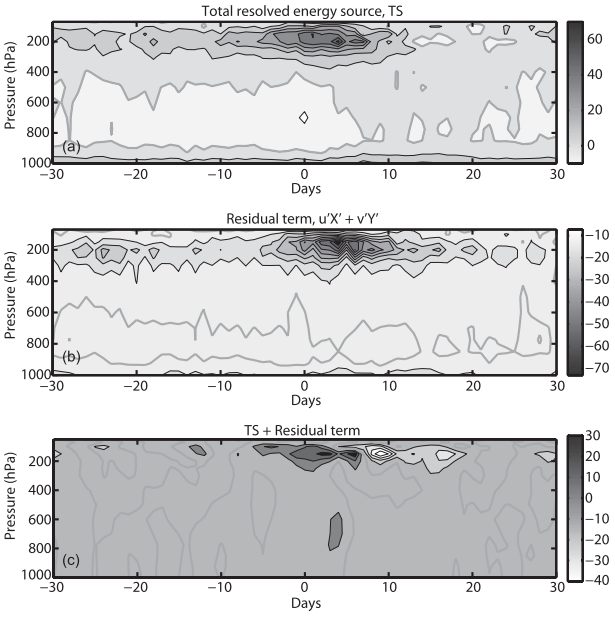


FIG. 12. As in Fig. 9, but for (a) TS [Eq. (3)], for (b) $u'X' + v'Y'$, and for (c) the sum of TS and $u'X' + v'Y'$ (units: J day$^{-1}$ kg$^{-1}$).

based on the decomposition in time are also the same as the corresponding terms in Eq. (2). However, the specific forms have some differences. For example, $\partial\overline{u}/\partial x$ in $\nabla\overline{u}$ for the decomposition in space is zero since the zonal mean is independent of $x$, while with the time mean, this term is not zero. Nevertheless, the above conclusions drawn from the spatial decomposition remain valid for the decomposition in time.

For example, the vertical profile of the energy conversion between PE′ and KE′ is shown with white contours in Fig. 13 and the vertical profile of the work done by PGF is shown with color shading in Fig. 13. The patterns in Fig. 13 are very similar to those in Fig. 10, which shows the counterpart for the decomposition in the zonal direction. Again, the dominant kinetic energy source at the MJO scale is from PE′, which ranges from 500 to 300 hPa. The kinetic energy gained from PE′ is redistributed by the work done by PGF, which shifts the energy both upward and downward and also shifts the energy to a few days after day 0 when the OLR anomalies reach their minima.

The westerly wind burst is not evident in Fig. 13. While perhaps counterintuitive, this result does not appear to contradict any fundamental principle or well-understood aspect of MJO dynamics. It indicates that, although the westerly wind burst contains much kinetic energy, it is not the site of kinetic energy production (or dissipation) comparable to that in the upper troposphere. The upper-tropospheric MJO easterlies appear to be strongly driven by conversion from potential to

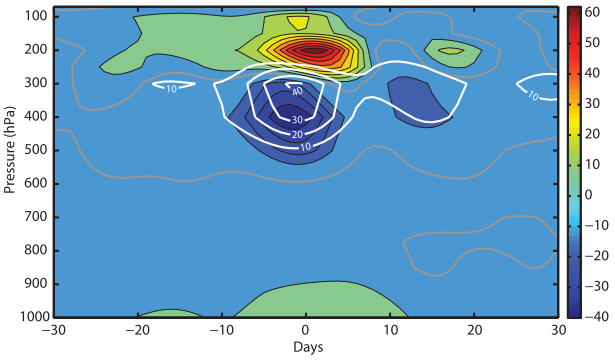


FIG. 13. As in Fig. 10, but for the decomposition with respect to time. [KE′ × PE′] with white contours and for $-\nabla\cdot(\mathbf{U}'\Phi')$ with color shading (units: J day$^{-1}$ kg$^{-1}$).

kinetic energy but also strongly damped, presumably by cumulus friction, while the lower-tropospheric westerlies are both less strongly driven and more nearly inviscid. The implied weaker dissipation in the lower troposphere may perhaps be surprising given its proximity to the surface. However, the calculations of CMT in a global cloud-permitting model by Miyakawa et al. (2012) suggest that CMT may actually accelerate the westerlies right near the surface and shift them westward

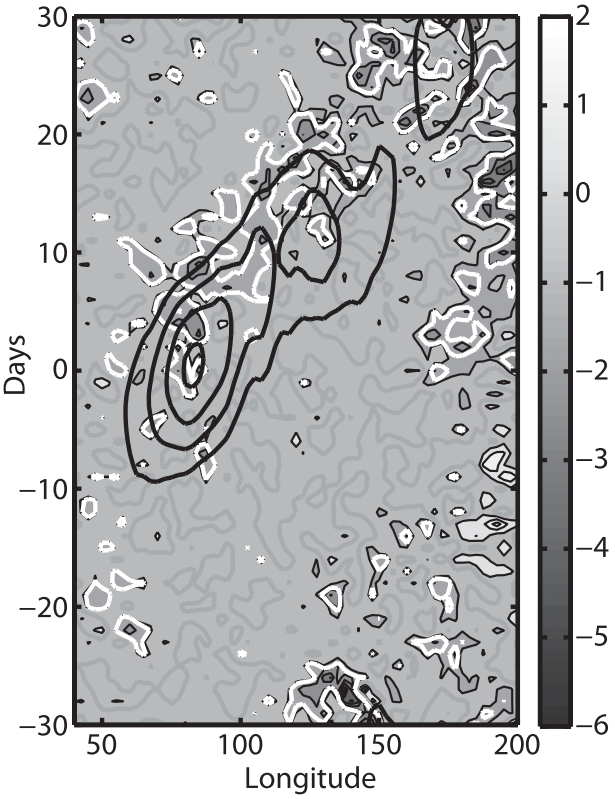


FIG. 14. As in Fig. 8, but for [KE′ × KE″] with the decomposition in time. The interval of thin black contours is 1 J day$^{-1}$ kg$^{-1}$.

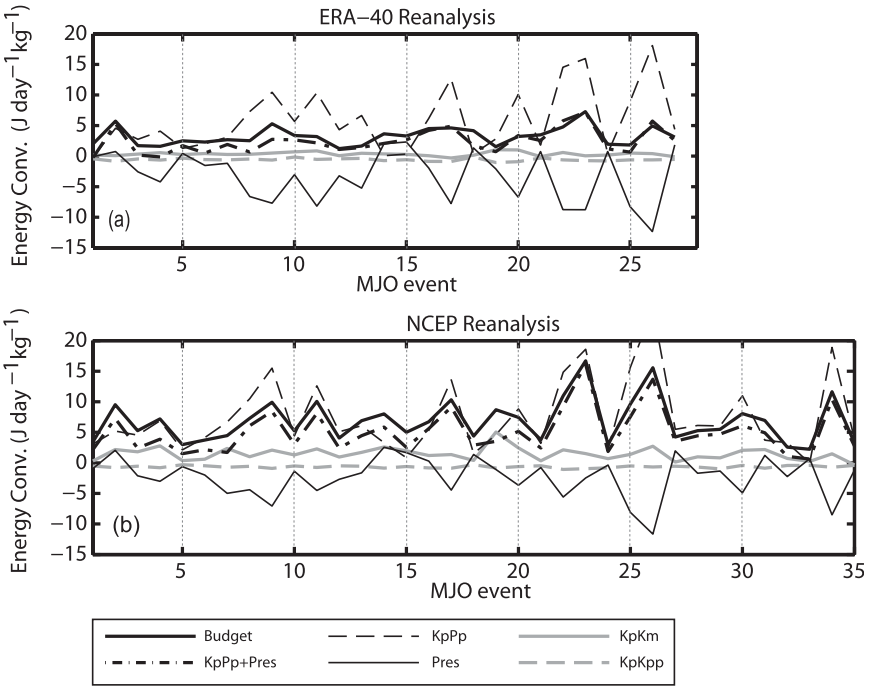


FIG. 15. (a) Major terms in the kinetic energy budget calculated with ERA-40. All terms are averaged horizontally within 10°N–10°S and 50°E–180°, vertically from 1000 and 100 hPa, and between day −10 and day 25 in time. Budget denotes TS [Eq. (3)], KpKm denotes $[KE' \times \overline{KE}]$, KpKpp denotes $[KE' \times KE'']$, KpPp denotes $[KE' \times PE']$, and Pres denotes $\nabla \cdot (\mathbf{U}'\Phi')$. (b) As in (a), but it is obtained with the NCEP reanalysis.

in the lower- and midtroposphere (rather than damping them overall) while damping the easterlies in the upper troposphere. This appears at least partly consistent with our results, recognizing that near the surface our residual includes both direct surface drag and CMT.

Figure 14 shows the kinetic energy exchange between KE′ and KE″ (obtained with the temporal decomposition rather than spatial decomposition), which is very similar to Fig. 8. The kinetic energy is transferred one way—from the intraseasonal band to the high-frequency band—to the west of the convection center during the whole lifetime of the composite MJO event. The similarity between the decomposition with two different ways demonstrates the robustness of our conclusions.

## 5. Case studies

As stated in the introduction, various mechanisms for the MJO have been proposed, focusing on various physical processes. In the previous section, we analyzed the composite kinetic energy budget and showed that the dominant terms in the kinetic energy budget are $[KE' \times PE']$, $-\nabla \cdot (\mathbf{U}'\Phi')$, and cumulus momentum transport. If one examines all MJO events listed in Table 1, this balance is valid for most of the individual MJO events, but the relative importance of different terms varies somewhat from one MJO event to another. For some events, the dominant balance can be different from that in the composite budget. The budget during a few events is dominated by the energy gain from the mean flow via the term $[KE' \times \overline{KE}]$, while a few other events are significantly influenced by the subtropics (mainly via $v'\Phi'$; see details below). In Fig. 15 (with both ERA-40 and NCEP reanalysis), major terms in the energy budget (averaged horizontally within 10°N–10°S and 50°E–180°, vertically from 1000 to 100 hPa, and between day −10 and day 25 in time, day 0 is when maximum convection occurs at 80°E) are shown for the MJO events listed in Table 1. For most MJO events, the energy gain from PE′ (thin black dash lines in Fig. 15) is the major energy source and is compensated by the work done by PGF (thick black solid lines in Fig. 15), which is mainly negative. The sum of these two dominant terms (dash–dot lines in Fig. 15) is very close to the total energy source (thick black solid lines in Fig. 15), which confirms again that this balance is the dominant balance during most MJO events. Nevertheless, there are several MJO events for which this balance does not hold. For example, $-\nabla \cdot (\mathbf{U}'\Phi')$ is positive during MJO events 14 and 15,

while the energy gained from PE′ is very small. Another example of the exception is MJO event 19, in which the energy gain from mean kinetic energy via $[\mathrm{KE}' \times \overline{\mathrm{KE}}]$ (thick gray solid lines in Fig. 15) dominates. Since there are only a few special events of these two kinds, it is not necessary to categorize them into different groups according to the dominant kinetic energy components. Instead, the two kinds of special cases are analyzed separately as case studies below.

### *a. MJO events with significant extratropical influence*

The extratropical influence on the MJO has been examined in many previous studies, such as Hsu et al. (1990), Matthews and Kiladis (1999), and Weickmann and Berry (2009). With the data obtained from the Tropical Ocean and Global Atmosphere (TOGA) Coupled Ocean–Atmosphere Response Experiment (COARE) Intensive Observing Period (during event 20 in Table 1), Yanai et al. (2000) reported strong horizontal energy convergence from the extratropics. Most recently, Ray and Zhang (2010) examined the extratropical influence in detail in one MJO event, namely, event 27 in Table 1. As shown in Fig. 15, the dominance of kinetic energy input from the extratropics is not common for most MJO events. Thus, such events are somewhat special.

One can integrate the term $-\nabla \cdot (\mathbf{U}'\phi')$ over a large domain, that is, $\int\int\int -[(\partial u'\phi'/\partial x) + (\partial v'\phi'/\partial y) + (\partial \omega'\phi'/\partial p)]\, dx\, dy\, dp$. The assumption that the vertical velocities are very small at the bottom (1000 hPa) and the top of the troposphere (100 hPa) is well satisfied in the reanalysis products (not shown). Thus, the vertical integration of $\partial \omega'\phi'/\partial p$ is very close to zero. Integrating along any latitude around the globe, $\oint (\partial u'\Phi'/\partial x)\, dx = 0$ is also well satisfied, since this integral is along a closed circle. Therefore, the integral of $-\nabla \cdot (\mathbf{U}'\phi')$ is determined by the meridional integration from the northern boundary to the southern boundary, that is, $\int_{\mathrm{SB}}^{\mathrm{NB}} -(\partial v'\Phi'/\partial y)\, dy = v'\Phi'|_{\mathrm{SB}} - v'\Phi'|_{\mathrm{NB}}$, where NB and SB represent the northern and the southern boundaries of the integration domain (e.g., 10°N and 10°S). Physically, $\int_{\mathrm{SB}}^{\mathrm{NB}} -(\partial v'\Phi'/\partial y)\, dy$ represents the influence of higher latitudes on the tropics. Figure 15 shows that MJO events 14, 15, 27 (discussed in Ray and Zhang 2010), and a few others have significant positive energy input from the extratropics. Some events of this kind also have relatively small energy gains from PE′, for example, MJO events 14 and 15 (Table 1). Accordingly, the negative work done by the PGF, which is needed to compensate $[\mathrm{KE}' \times \mathrm{PE}']$, is also small. However, the significant influence from the extratropics leads to positive values of $-\nabla \cdot (\mathbf{U}'\phi')$ and accounts for a major portion of TS [Eq. (3)] during these two events. The vertical profiles of mean $-\partial v'\phi'/\partial y$ averaged between 10°N and 10°S at 80°E are shown in Fig. 16. The composite profiles over all MJO events are shown in Fig. 16a and the averaged profiles during these two MJO events (14 and 15 in Table 1) are shown in Fig. 16b. These profiles share some qualitative features, such as the negative values in the upper troposphere (~200 hPa) and at the lower troposphere (between 800 to 600 hPa), which are suggestive of wave radiation to higher latitudes. However, because of the meridional cell between the tropics and the subtropics (Ray and Zhang 2010; Lin et al. 2007), there are some differences in the upper troposphere. For example, negative values are found from day −10 to day 5 in the composite MJO event (Fig. 16a), but from day 0 to day 10 in Fig. 16b. In addition, positive values are found from day −10 to day 0 in Fig. 16b. However, the most distinct difference resides below 800 hPa. There are pronounced positive values in events 14 and 15, while during the composite MJO event the meridional average of $-\partial v'\phi'/\partial y$ between the northern and the southern boundaries is close to zero.

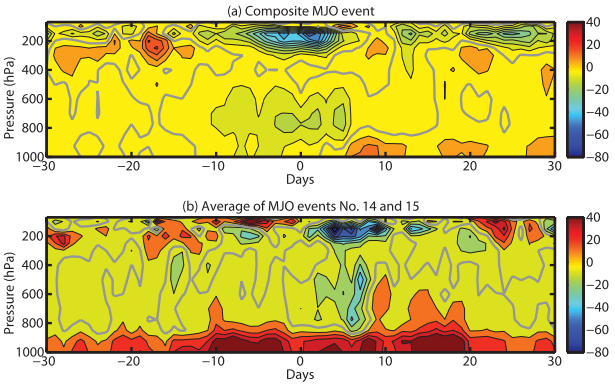


FIG. 16. As in Fig. 9, but for $-\partial v'\Phi'/\partial y$ averaged between 10°N and 10°S. (top) Obtained for the composite MJO event. (bottom) The average of the MJO events 14 and 15 in Table 1 (units: J day$^{-1}$ kg$^{-1}$).

### *b. MJO events in which conversion from* $\overline{\mathrm{KE}}$ *dominates*

As shown in Fig. 15, for a few MJO events, the energy gain from the mean kinetic energy via $[\mathrm{KE}' \times \overline{\mathrm{KE}}]$ dominates, such as 4 and 19 (comparing the thick gray solid lines and the thick black solid lines in Fig. 15). The explicit form of $[\mathrm{KE}' \times \overline{\mathrm{KE}}]$ is $-u'(\mathbf{U}' \cdot \nabla \overline{u}) - v'(\mathbf{U}' \cdot \nabla v')$. Thus, the energy conversion between KE′ and $\overline{\mathrm{KE}}$ is closely related to both horizontal and vertical shears of the background winds. Note $\partial \overline{u}/\partial x$ is zero for the decomposition in the zonal direction, but it is not zero for the decomposition in time (in which case the overbar represents a time average). The energy conversion from zonal mean wind shear is associated with barotropic

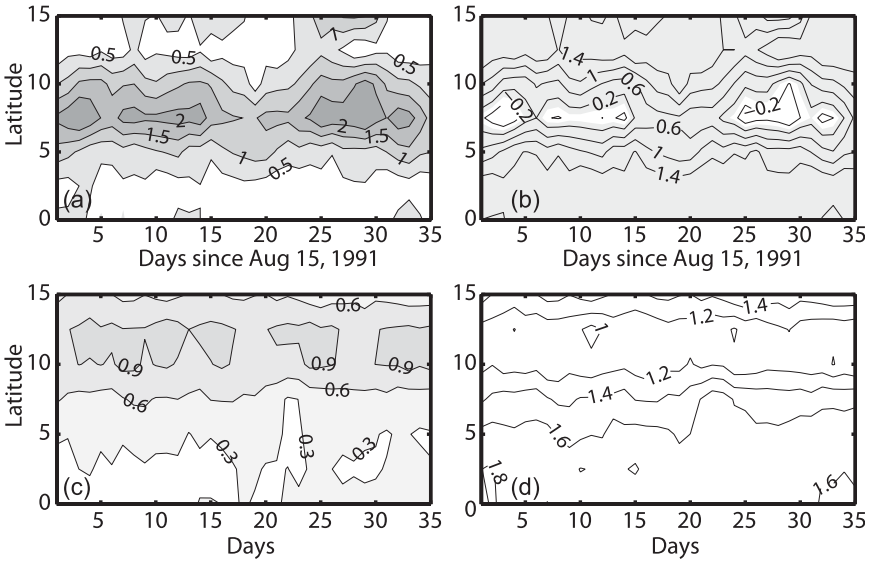


FIG. 17. The (a) $|\overline{U}_{yy}|$ and (b) $\beta - |\overline{U}_{yy}|$ at 850 hPa during one special MJO event. (c),(d) As in (a),(b) respectively, but for the composite MJO event (units: $10^{-11}$ m$^{-1}$ s$^{-1}$). Positive values in (b) are shaded. All values in (d) are positive.

instability or nonmodal growth. These mechanisms are usually hypothesized to be relevant to synoptic-scale tropical disturbances (e.g., Nitta and Yanai 1969; Webster and Chang 1988; Ferreira and Schubert 1997; Sobel and Bretherton 1999; Maloney and Hartmann 2001; Wang and Magnusdottir 2006; Seiki and Takayabu 2007), rather than the MJO per se. Current analysis focuses on the region from the mid-Indian Ocean to the western Pacific Ocean (from 80° to 130°E in the Hovmöller diagram such as Fig. 7). A detailed study on the ingredients in $[\mathrm{KE}' \times \overline{\mathrm{KE}}]$ (e.g., the relative importance of $\partial\overline{u}/\partial x$ and $\partial\overline{u}/\partial y$ along the lines of the discussion in Maloney and Hartmann 2001) will be carried out in the future. Nevertheless, the possibility that the barotropic instability is critical for the special events listed above can be tested by examining the necessary condition for the barotropic instability, that is, whether $dq/dy = \beta - |\partial^2\overline{U}/\partial y^2|$ [where $q$ is the quasigeostrophic potential vorticity (QGPV), $\beta$ is the meridional gradient of the Coriolis parameter, and $\overline{U}$ is the background mean flow] changes sign in the study area. Between 5° and 10°N, the meridional shear in zonal winds is enhanced from 15 August 1991 to 18 September 1991 (event 19 in Table 1; Fig. 17a). The large meridional gradient of the background flow overcomes the $\beta$ effect and leads to negative $dq/dy$ during this MJO event (Fig. 17b). The energy gain of KE′ from $\overline{\mathrm{KE}}$ is also pronounced in the lower troposphere during this event (not shown). Therefore, it is possible that the necessary condition for barotropic instability is satisfied in this region. Whether any unstable waves potentially generated by this instability can contribute on the MJO scale requires further study. Nevertheless, considering the energy conversion calculated with the energy budget equation above, we can speculate that barotropic instability may contribute to the generation of KE′ during this MJO event. For comparison, one can consider the composite MJO event (event 19, which is shown in Figs. 17a and 17b, is included in the composite event, but inclusion or exclusion of a specific event does not make notable difference to the composite), in which the energy gain from $\overline{\mathrm{KE}}$ is not pronounced. As shown in Fig. 17c, during the composite MJO event, the meridional gradients of zonal winds are much smaller than they are in Fig. 17a. As a result, positive $dq/dy$ is found everywhere over all regions, indicating that the meridional gradient of zonal winds is too weak to overcome $\beta$ (Fig. 17d) and thus barotropic instability cannot occur. For this class of MJO events, since the energy is mainly obtained from the mean kinetic energy, large gradients of horizontal winds are a necessary ingredient.

## 6. Conclusions and discussion

In this study, the MJO is examined from the kinetic energy point of view. The kinetic energy budget is established in a three-scale framework, with a focus on the MJO scale. The dominant processes are synthesized in the sketch in Fig. 18. In the composite kinetic energy budget, the major balance at the MJO scale (KE′) is between gain from the potential energy at the same scale (PE′) and the work done by the PGF, which serves to move KE′ away from the region of generation to nearby

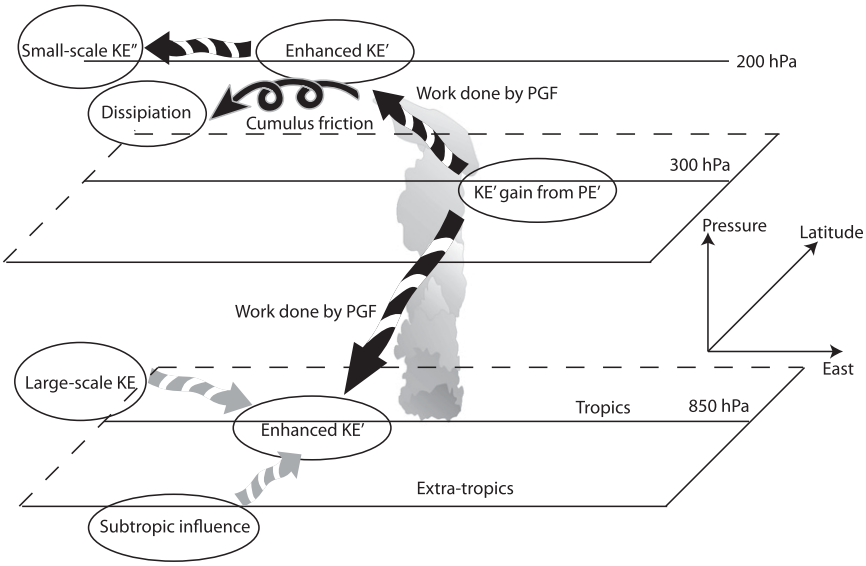


FIG. 18. Sketch for the energy conversions on the MJO scale. Black arrows denote the dominant processes for most MJO events or the composite event, while gray arrows denote processes that are only significant for a few special MJO events.

regions. This balance is qualitatively consistent with that in the classical linear Gill model. The major energy balance for the composite MJO event (namely conversion from PE′ around 300 hPa and transfer to upper and lower troposphere by PGF) is similar to previous studies on tropical synoptic-scale disturbances (e.g., Nitta 1972; Lau and Lau 1992; Seiki and Takayabu 2007), although the MJO is quite different from those synoptic-scale disturbances in many respects. A considerable amount of kinetic energy appears to dissipate near the tropopause because of cumulus friction, which is consistent with previous observations such as Tung and Yanai (2002).

The energy budget in a three-scale framework is able to explicitly display the energy transfer between the MJO and the adjacent scales (the zonal mean scale and the small scale of hundred kilometers). The results show that kinetic energy exchanges between different scales are not important in a typical MJO event, as represented by our composites. Exchange of kinetic energy with the synoptic scale (KE″) is a modest-amplitude sink of MJO-scale kinetic energy, KE′. The KE″ absorbs kinetic energy from KE′ a few days after the deep convection during MJO events. This conclusion supports that the synoptic disturbances are strengthened because of the intraseasonal variabilities (Maloney and Dickinson 2003). But it does not obviously support the hypothesis that the upscale transfers from KE″ to KE′ are critical to the generation of kinetic energy during most MJO events. The caveat here is that we do not show the potential energy budget during the MJO because of the lack of key variables (e.g., the diabatic heating). The energy transfer from PE″ to PE′ seems to be significantly positive before the convection. As a result, the upscale energy transfer from PE″ to PE′ may also be important to explain the pronounced PE′, which is then converted to KE′. In this way, the upscale energy transfer from the synoptic scale to the MJO scale may be important to the MJO. But this hypothesis needs more quantitative studies in the future.

In the vertical profile, the conversion from PE′ to KE′ occurs between 500 and 200 hPa, which is consistent with the release of latent heat in the upper troposphere. The obtained kinetic energy is shifted both upward to above 200 hPa and downward to the lower troposphere by the PGF. For the composite MJO event, all energy conversion terms are large in the upper troposphere but small in the lower troposphere. However, for a specific MJO event, the energy conversion can be significant in the lower troposphere. For example, the energy gain from $\overline{\mathrm{KE}}$ is pronounced in the lower troposphere during MJO event 19 (Table 1), which is discussed in section 5b. The energy gain from the barotropic energy conversion in the lower troposphere was also discussed in Seiki and Takayabu (2007).

Although most MJO events share a similar partitioning between dominant terms in the kinetic energy equation, some MJO events have different balances in the kinetic energy budget from the balance for the composite event. A few events are significantly influenced by barotropic conversion from the background winds while others are significantly influenced by energy input from the extratropics, which is consistent with the previous case study in Ray and Zhang (2010). Such kind of MJO events usually

occur in monsoon transition season, which is consistent with the analysis by Maloney and Dickinson (2003).

*Acknowledgments.* Zhou gratefully acknowledges NOAA Climate and Global Change Postdoctoral Fellowship Program. Zhou is also thankful for the traveling funding support from Open Fund of State Key Lab of Satellite Ocean Environment Dynamics, SIO, SOA, under Contract SOED1005. We thank three anonymous reviewers for helpful and insightful comments. RM acknowledges the ONR DYNAMO grant.

## APPENDIX A

### Decomposition of Advection Terms

Take the following simple zonal momentum equation as an example:

$$\frac{\partial u}{\partial t} + u\frac{\partial u}{\partial x} + v\frac{\partial u}{\partial y} - fv = -\frac{\partial \Phi}{\partial x}, \tag{A1}$$

where all notations are the same as used in Eq. (1). If all variables are decomposed into two components, that is, the zonal mean and the perturbation, Eq. (A1) becomes

$$\frac{\partial(\overline{u} + u')}{\partial t} + (\overline{u} + u')\frac{\partial(\overline{u} + u')}{\partial x} + (\overline{v} + v')\frac{\partial(\overline{u} + u')}{\partial y} - f(\overline{v} + v') = -\frac{\partial(\overline{\Phi} + \Phi')}{\partial x}. \tag{A2}$$

The equation for the zonal mean part is

$$\frac{\partial \overline{u}}{\partial t} + \overline{u}\frac{\partial \overline{u}}{\partial x} + \overline{u'\frac{\partial u'}{\partial x}} + \overline{v}\frac{\partial \overline{u}}{\partial y} + \overline{v'\frac{\partial u'}{\partial y}} - f\overline{v} = -\frac{\partial \overline{\Phi}}{\partial x}. \tag{A3}$$

The difference between Eq. (A2) and Eq. (A3) gives the perturbation equation,

$$\frac{\partial u'}{\partial t} + \overline{u}\frac{\partial u'}{\partial x} + u'\frac{\partial u'}{\partial x} + \left(u'\frac{\partial u'}{\partial x} - \overline{u'\frac{\partial u'}{\partial x}}\right) + \overline{v}\frac{\partial u'}{\partial y} + v'\frac{\partial \overline{u}}{\partial y} + \left(v'\frac{\partial u'}{\partial y} - \overline{v'\frac{\partial u'}{\partial y}}\right) - fv' = -\frac{\partial \Phi'}{\partial x}. \tag{A4}$$

The products of two perturbation terms, that is, $\overline{u'\partial u'/\partial x}$ and $\overline{v'\partial u'/\partial y}$ which is the upscale transport from the perturbation to the mean, belong to the equation at the background scale, which is larger than the perturbation scale.

For the decomposition with three scales, taking $v\partial u/\partial y$ for example, one obtains

$$(\overline{v} + v' + v'')\frac{\partial(\overline{u} + u' + u'')}{\partial y}. \tag{A5}$$

Taking the zonal average, since $\overline{()'} = 0$ and $\overline{()''} = 0$, the nonzero terms (which are also the terms belonging to the zonal mean momentum equation) are

$$\overline{v}\frac{\partial \overline{u}}{\partial y} + \overline{v'\frac{\partial u'}{\partial y}} + \overline{v''\frac{\partial u''}{\partial y}}. \tag{A6}$$

Then, subtract Eq. (A6) from Eq. (A5) and one has

$$\overline{v}\frac{\partial u'}{\partial y} + \overline{v}\frac{\partial u''}{\partial y} + v'\frac{\partial \overline{u}}{\partial y} + v'\frac{\partial u''}{\partial y} + v''\frac{\partial \overline{u}}{\partial y} + v''\frac{\partial u'}{\partial y} + \left(v'\frac{\partial u'}{\partial y} - \overline{v'\frac{\partial u'}{\partial y}}\right) + v''\frac{\partial u''}{\partial y}. \tag{A7}$$

Note that the nonlinear term $v''\partial u''/\partial y$ also has a projection at the zonal mean scale. Therefore, strictly speaking, it should be $v''\partial u''/\partial y - \overline{v''\partial u''/\partial y}$ in Eq. (A7). However, one can ensure with reanalysis products that $\overline{v''\partial u''/\partial y}$ is much smaller than $v''\partial u''/\partial y$ (not shown). Physically, it is equivalent to assuming that the energy cascade is local in scale and the energy cannot transfer from one scale (e.g., the small scale with a double prime) to another scale (e.g., the zonal mean scale with a bar), which is not adjacent to the former one. Therefore, $\overline{v''\partial u''/\partial y}$ is neglected in Eq. (A7). Taking the average of Eq. (A7) at the MJO scale, which is denoted as [ ], since $[()''] = 0$, the nonzero terms, which belong to the momentum equation at the MJO scales, are

$$\left[\overline{v}\frac{\partial u'}{\partial y}\right] + \left[v'\frac{\partial \overline{u}}{\partial y}\right] + \left[v''\frac{\partial u''}{\partial y}\right] + \left(\left[v'\frac{\partial u'}{\partial y}\right] - \overline{v'\frac{\partial u'}{\partial y}}\right). \tag{A8}$$

Finally, the remaining terms, which belong to the momentum equation at the small scale, are

$$\overline{v}\frac{\partial u''}{\partial y} + v'\frac{\partial u''}{\partial y} + v''\frac{\partial \overline{u}}{\partial y} + v''\frac{\partial u'}{\partial y} + \left(v''\frac{\partial u''}{\partial y} - \left[v''\frac{\partial u''}{\partial y}\right]\right). \tag{A9}$$

Therefore, the major advection terms as a result of the decomposition with three scales can be assumed to be (taking $v\partial u/\partial y$ for example) the following:

1) equation at the background scale includes $\overline{v}\partial\overline{u}/\partial y$ and $\overline{v'\partial u'/\partial y}$;
2) advection at the MJO scale consists of $[\overline{v}\partial u'/\partial y]$, $[v'\partial u/\partial y]$, $[v''\partial u''/\partial y]$, and $[v'\partial u'/\partial y] - \overline{v'\partial u'/\partial y}$ and
3) small-scale advection is comprised of $\overline{v}\partial u''/\partial y$, $v''\partial\overline{u}/\partial y$, $v'\partial u''/\partial y$, $v''\partial u'/\partial y$, and $v''\partial u''/\partial y - [v''\partial u''/\partial y]$.

Since we focus on the MJO scale in current study, the advection terms on the background scale and the small scale are not used in the main text.

## APPENDIX B

### Derivation of Eq. (2)

After decomposition, the governing equations [Eq. (1)] for the MJO scale can be written as

$$\frac{\partial u'}{\partial t} + \overline{u}\frac{\partial u'}{\partial x} + u''\frac{\partial u''}{\partial x} + \left(u'\frac{\partial u'}{\partial x} - \overline{u'\frac{\partial u'}{\partial x}}\right) + \overline{v}\frac{\partial u'}{\partial y} + v'\frac{\partial \overline{u}}{\partial y} + v''\frac{\partial u''}{\partial y} + \left(v'\frac{\partial u'}{\partial y} - \overline{v'\frac{\partial u'}{\partial y}}\right) + \overline{\omega}\frac{\partial u'}{\partial p} + \omega'\frac{\partial \overline{u}}{\partial p} + \omega''\frac{\partial u''}{\partial p} + \left(\omega'\frac{\partial u'}{\partial p} - \overline{\omega'\frac{\partial u'}{\partial p}}\right) - \beta y v' = -\frac{\partial \Phi'}{\partial p} + X', \tag{B1a}$$

$$\frac{\partial v'}{\partial t} + \overline{u}\frac{\partial v'}{\partial x} + u''\frac{\partial v''}{\partial x} + \left(u'\frac{\partial v'}{\partial x} - \overline{u'\frac{\partial v'}{\partial x}}\right) + \overline{v}\frac{\partial v'}{\partial y} + v'\frac{\partial \overline{v}}{\partial y} + v''\frac{\partial v''}{\partial y} + \left(v'\frac{\partial v'}{\partial y} - \overline{v'\frac{\partial v'}{\partial y}}\right) + \overline{\omega}\frac{\partial v'}{\partial p} + \omega'\frac{\partial \overline{v}}{\partial p} + \omega''\frac{\partial v''}{\partial p} + \left(\omega'\frac{\partial v'}{\partial p} - \overline{\omega'\frac{\partial v'}{\partial p}}\right) - \beta y u' = -\frac{\partial \Phi'}{\partial p} + Y', \tag{B1b}$$

$$\frac{\partial u'}{\partial x} + \frac{\partial v'}{\partial y} + \frac{\partial \omega'}{\partial p} = 0, \quad \text{and} \tag{B1c}$$

$$\frac{\partial \Phi'}{\partial p} = -\frac{RT'}{p}. \tag{B1d}$$

Applying $u' \times$ Eq. (B1a) + $v' \times$ Eq. (B1b) and with the help of continuity equation, one can obtain

$$\left(\frac{\partial}{\partial t} + \mathbf{U}\cdot\nabla\right)\left(\frac{u'^2 + v'^2}{2}\right) + [u'\nabla(u''\mathbf{U}'') + v'\nabla(v''\mathbf{U}'')] + [u'(\mathbf{U}'\cdot\nabla\overline{u}) + v'(\mathbf{U}'\cdot\nabla v')] + u'\left[\left(u'\frac{\partial u'}{\partial x} - \overline{u'\frac{\partial u'}{\partial x}}\right) + \left(v'\frac{\partial u'}{\partial y} - \overline{v'\frac{\partial u'}{\partial y}}\right) + \left(\omega'\frac{\partial u'}{\partial p} - \overline{\omega'\frac{\partial u'}{\partial p}}\right)\right] + v'\left[\left(u'\frac{\partial v'}{\partial x} - \overline{u'\frac{\partial v'}{\partial x}}\right) + \left(v'\frac{\partial v'}{\partial y} - \overline{v'\frac{\partial v'}{\partial y}}\right) + \left(\omega'\frac{\partial v'}{\partial p} - \overline{\omega'\frac{\partial v'}{\partial p}}\right)\right] = -u'\frac{\partial \Phi'}{\partial x} - v'\frac{\partial \Phi'}{\partial y} + u'X' + v'Y'. \tag{B2}$$

Adding the equation $-\Phi'(\partial u'/\partial x) - \Phi'(\partial v'/\partial y) - \Phi'(\partial \omega'/\partial p) = 0$ to Eq. (B2) and using Eq. (B1d) one can obtain Eq. (2) in the main text, that is, the kinetic energy equation at the MJO scale.

## REFERENCES


Biello, J. A., and A. J. Majda, 2005: A new multiscale model for the Madden–Julian oscillation. *J. Atmos. Sci.,* **62,** 1694–1721.

——, ——, and M. W. Moncrieff, 2007: Meridional momentum flux and superrotation in the multiscale IPESD MJO model. *J. Atmos. Sci.,* **64,** 1636–1651.

Blade, I., and D. L. Hartmann, 1993: Tropical intraseasonal oscillations in a simple nonlinear model. *J. Atmos. Sci.,* **50,** 2922–2939.

Bretherton, C. S., and A. H. Sobel, 2003: The Gill model and the weak temperature gradient approximation. *J. Atmos. Sci.,* **60,** 451–460.

Emanuel, K. A., 1987: An air–sea interaction model of intraseasonal oscillations in the tropics. *J. Atmos. Sci.,* **44,** 2324–2340.

Ferreira, R. N., and W. H. Schubert, 1997: Barotropic aspects of ITCZ breakdown. *J. Atmos. Sci.,* **54,** 261–285.

Gill, A. E., 1980: Some simple solutions for heat-induced tropical circulation. *Quart. J. Roy. Meteor. Soc.,* **106,** 447–462.

Hendon, H. H., and M. L. Salby, 1994: The life cycle of the Madden–Julian oscillation. *J. Atmos. Sci.,* **51,** 2225–2237.

Holton, J. R., 2004: *An Introduction to Dynamic Meteorology.* 4th ed. Academic Press, 535 pp.

Houze, R. A., Jr., 1982: Cloud clusters and large-scale vertical motions in the tropics. *J. Meteor. Soc. Japan,* **60,** 396–409.

Hsu, H.-H., B. J. Hoskins, and F.-F. Jin, 1990: The 1985/86 intraseasonal oscillation and the role of the extratropics. *J. Atmos. Sci.,* **47,** 823–839.

Hu, Q., and D. A. Randall, 1995: Low-frequency oscillations in radiative convective systems 2. An idealized model. *J. Atmos. Sci.,* **52,** 478–490.

Kalnay, E., and Coauthors, 1996: The NCEP/NCAR 40-Year Reanalysis Project. *Bull. Amer. Meteor. Soc.,* **77,** 437–471.

Kemball-Cook, S. R., and B. C. Weare, 2001: The onset of convection in the Madden–Julian oscillation. *J. Climate,* **14,** 780–793.

Kiladis, G. N., M. C. Wheeler, P. T. Haertel, K. H. Straub, and P. E. Roundy, 2009: Convectively coupled equatorial waves. *Rev. Geophys.,* **47,** RG2003, doi:10.1029/2008RG000266.

Lau, K.-H., and N.-C. Lau, 1992: The energetics and propagation dynamics of tropical summertime synoptic-scale disturbances. *Mon. Wea. Rev.,* **120,** 2523–2539.

Lau, K. M., and L. Peng, 1987: Origin of low-frequency (intraseasonal) oscillations in the tropical atmosphere 1. Basic theory. *J. Atmos. Sci.,* **44,** 950–972.

Leith, C. E., 1973: The standard error of time-average estimates of climatic means. *J. Appl. Meteor.,* **12,** 1066–1069.

Lin, H., G. Brunet, and J. Derome, 2007: Intraseasonal variability in a dry atmospheric model. *J. Atmos. Sci.,* **64,** 2422–2441.

Lin, J. L., M. H. Zhang, and B. Mapes, 2005: Zonal momentum budget of the Madden–Julian oscillation: The source and strength of equivalent linear damping. *J. Atmos. Sci.,* **62,** 2172–2188.

Lindzen, R. S., 1974: Wave–CISK in tropics. *J. Atmos. Sci.,* **31,** 156–179.

Lorenz, E. N., 1955: Available potential energy and the maintenance of the general circulation. *Tellus,* **7,** 157–167.

Madden, R. A., and P. R. Julian, 1971: Detection of a 40–50-day oscillation in zonal wind in tropical Pacific. *J. Atmos. Sci.,* **28,** 702–708.

——, and ——, 1972: Description of global-scale circulation cells in tropics with a 40–50-day period. *J. Atmos. Sci.,* **29,** 1109–1123.

——, and ——, 1994: Observations of the 40–50-day tropical oscillation—A review. *Mon. Wea. Rev.,* **122,** 814–837.

Majda, A. J., 2007a: New multiscale models and self-similarity in tropical convection. *J. Atmos. Sci.,* **64,** 1393–1404.

——, 2007b: Multiscale models with moisture and systematic strategies for superparameterization. *J. Atmos. Sci.,* **64,** 2726–2734.

Maloney, E. D., and D. L. Hartmann, 2001: The Madden–Julian oscillation, barotropic dynamics, and North Pacific tropical cyclone formation. Part I: Observations. *J. Atmos. Sci.,* **58,** 2545–2558.

——, and M. J. Dickinson, 2003: The intraseasonal oscillation and the energetics of summertime tropical western North Pacific synoptic-scale disturbances. *J. Atmos. Sci.,* **60,** 2153–2168.

Matthews, A. J., 2008: Primary and successive events in the Madden–Julian oscillation. *Quart. J. Roy. Meteor. Soc.,* **134,** 439–453.

——, and G. N. Kiladis, 1999: The tropical–extratropical interaction between high-frequency transients and the Madden–Julian oscillation. *Mon. Wea. Rev.,* **127,** 661–677.

Milliff, R. F., J. Morzel, D. B. Chelton, and M. H. Freilich, 2004: Wind stress curl and wind stress divergence biases from rain effects on QSCAT surface wind retrievals. *J. Atmos. Oceanic Technol.,* **21,** 1216–1231.

Miyakawa, T., Y. N. Takayabu, T. Nasuno, H. Miura, M. Satoh, and M. Moncrieff, 2012: Convective momentum transport by rainbands within a Madden–Julian oscillation in a global nonhydrostatic model with explicit deep convective processes. Part I: Methodology and general results. *J. Atmos. Sci.,* **69,** 1317–1338.

Moncrieff, M. W., 2004: Analytic representation of the large-scale organization of tropical convection. *J. Atmos. Sci.,* **61,** 1521–1538.

Neelin, J. D., I. M. Held, and K. H. Cook, 1987: Evaporation–wind feedback and low-frequency variability in the tropical atmosphere. *J. Atmos. Sci.,* **44,** 2341–2348.

Nitta, T., 1972: Energy budget of wave disturbances over the Marshall Islands during the years of 1956 and 1958. *J. Meteor. Soc. Japan,* **50,** 71–84.

——, and M. Yanai, 1969: A note on the barotropic instability of the tropical easterly current. *J. Meteor. Soc. Japan,* **47,** 127–130.

Ray, P., and C. D. Zhang, 2010: A case study of the mechanics of extratropical influence on the initiation of the Madden–Julian oscillation. *J. Atmos. Sci.,* **67,** 515–528.

Raymond, D. J., 2001: A new model of the Madden–Julian oscillation. *J. Atmos. Sci.,* **58,** 2807–2819.

Schumacher, C., R. A. Houze, and I. Kraucunas, 2004: The tropical dynamical response to latent heating estimates derived from the TRMM precipitation radar. *J. Atmos. Sci.,* **61,** 1341–1358.

Seiki, A., and Y. N. Takayabu, 2007: Westerly wind bursts and their relationship with intraseasonal variations and ENSO. Part II: Energetics over the western and central pacific. *Mon. Wea. Rev.,* **135,** 3346–3361.

Slingo, J. M., P. M. Inness, and K. R. Sperber, 2005: Modeling. *Intraseasonal Variability in the Atmosphere-Ocean Climate System,* W. K. M. Lau and D. Waliser, Eds., Springer-Praxis, 361–388.

Sobel, A. H., and C. S. Bretherton, 1999: Development of synoptic-scale disturbances over the summertime tropical northwest Pacific. *J. Atmos. Sci.,* **56,** 3106–3127.

——, and H. Gildor, 2003: A simple time-dependent model of SST hot spots. *J. Climate,* **16,** 3978–3992.

——, and E. D. Maloney, 2012: An idealized semi-empirical framework for modeling the Madden-Julian oscillation. *J. Atmos. Sci.,* **69,** 1691–1705.

——, ——, G. Bellon, and D. M. Frierson, 2008: The role of surface heat fluxes in tropical intraseasonal oscillations. *Nat. Geosci.,* **1,** 653–657.

——, ——, ——, and ——, 2010: Surface fluxes and tropical intraseasonal variability: A reassessment. *J. Adv. Model Earth Syst.,* **2,** doi:10.3894/JAMES.2010.2.2.

Sugiyama, M., 2009: The moisture mode in the quasi-equilibrium tropical circulation model. Part I: Analysis based on the weak temperature gradient approximation. *J. Atmos. Sci.,* **66,** 1507–1523.

Taylor, G. I., 1921: Diffusion by continuous movement. *Proc. London Math. Soc.,* **21,** 196–212.

Tung, W. W., and M. Yanai, 2002: Convective momentum transport observed during the TOGA COARE IOP. Part I: General features. *J. Atmos. Sci.,* **59,** 1857–1871.

Uppala, S. M., and Coauthors, 2005: The ERA-40 Re-Analysis. *Quart. J. Roy. Meteor. Soc.,* **131,** 2961–3012.

Wang, B., 2005: Theory. *Intraseasonal Variability in the Atmosphere-Ocean Climate System,* W. K. M. Lau and D. Waliser, Eds., Springer-Praxis, 307–360.

——, and H. Rui, 1990: Synoptic climatology of transient tropical intraseasonal convection anomalies—1975–1985. *Meteor. Atmos. Phys.,* **44,** 43–61.

Wang, C.-C., and G. Magnusdottir, 2006: The ITCZ in the central and eastern Pacific on synoptic time scales. *Mon. Wea. Rev.,* **134,** 1405–1421.

Webster, P. J., and H.-R. Chang, 1988: Equatorial energy accumulation and emanation regions: Impacts of a zonally varying basic state. *J. Atmos. Sci.,* **45,** 803–829.

Weickmann, K., and E. Berry, 2009: The tropical Madden–Julian oscillation and the global wind oscillation. *Mon. Wea. Rev.,* **137,** 1601–1614.

Wheeler, M. C., and H. H. Hendon, 2004: An all-season real-time multivariate MJO index: Development of an index for monitoring and prediction. *Mon. Wea. Rev.,* **132,** 1917–1932.

Yanai, M., B. Chen, and W. W. Tung, 2000: The Madden–Julian oscillation observed during the TOGA COARE IOP: Global view. *J. Atmos. Sci.,* **57,** 2374–2396.

Zhang, C. D., 2005: Madden–Julian oscillation. *Rev. Geophys.,* **43,** RG2003, doi:10.1029/2004RG000158.

Zhou, L., R. Neale, M. Jochum, and R. Murtugudde, 2012: Improved Madden–Julian oscillations with improved physics: The impact of modified convection parameterizations. *J. Climate,* **25,** 1116–1136.